The Super Tuesday Outbreak: Forecast Sensitivities to Single-Moment Microphysics Schemes

Andrew L. Molthan[1,2], Jonathan L. Case[3], Scott R. Dembek[4], Gary J. Jedlovec[1], and William M. Lapenta[5]

[1]*NASA/MSFC Short-term Prediction Research and Transition (SPoRT) Center*

[2]*University of Alabama in Huntsville, Huntsville, AL*

[3]*ENSCO Inc./SPoRT Center*

[4]*Universities Space Research Association/SPoRT Center, Huntsville, AL*

[5]*NOAA/NWS/NCEP Environmental Modeling Center, Camp Springs, MD*

1. Introduction

Forecast precipitation and radar characteristics are used by operational centers to guide the issuance of advisory products. As operational numerical weather prediction is performed at increasingly finer spatial resolution, convective precipitation traditionally represented by sub-grid scale parameterization schemes is now being determined explicitly through single- or multi-moment bulk water microphysics routines. Gains in forecasting skill are expected through improved simulation of clouds and their microphysical processes. High resolution model grids and advanced parameterizations are now available through steady increases in computer resources. As with any parameterization, their reliability must be measured through performance metrics, with errors noted and targeted for improvement. Furthermore, the use of these schemes within an operational framework requires an understanding of limitations and an estimate of biases so that forecasters and model development teams can be aware of potential errors.

The National Severe Storms Laboratory (NSSL) Spring Experiments have produced daily, high resolution forecasts used to evaluate forecast skill among an ensemble with varied physical parameterizations and data assimilation techniques (Kain et al. 2008). In this research, high resolution forecasts of the 5-6 February 2008 Super Tuesday Outbreak are replicated using the NSSL configuration in order to evaluate two components of simulated convection on a large domain: sensitivities of quantitative precipitation forecasts to assumptions within a single-moment bulk water microphysics scheme, and to determine if these schemes accurately depict the reflectivity characteristics of well-simulated, organized, cold frontal convection. As radar returns are sensitive to the amount of hydrometeor mass and the distribution of mass among variably sized targets, radar comparisons may guide potential improvements to a single-moment scheme (Lang et al. 2007). In addition, object-based verification metrics are evaluated for their utility in gauging model performance and QPF variability.

Corresponding author: Andrew L. Molthan, NASA Marshall Space Flight Center, Huntsville, Alabama. E-mail: andrew.molthan@nasa.gov.

2. Background

Two single-moment schemes are used here in forecasts of the February 5-6 Super Tuesday Outbreak (Carbin and Schaefer 2008): the NASA Goddard (Tao et al. 2008; GSFC hereafter) and the Weather Research and Forecasting (WRF) model Six-Class Single-Moment (Hong and Lim 2006 and Hong et al. 2004; WSM6 hereafter) microphysics schemes. These schemes are limited to prognostic equations for the mixing ratios (or mass content) of six hydrometeor classes: water vapor, cloud water, cloud ice, rain, snow and graupel or hail. Each scheme is responsible for the representation of physical processes through formulas that quantify the growth or decay of each class.

The WSM6 and GSFC schemes are based upon the fundamental processes and equations described by Lin et al. (1983) and Rutledge and Hobbs (1983). Both use an inverse exponential size distribution for rain, snow and graupel. The inverse exponential distribution determines the volume concentration of a spherical diameter particle as a function of an intercept n_{ox} $(m^{-1}m^{-3})$ and slope parameter λ_x (m^{-1}), where "x" represents a hydrometeor category: $n(D) = n_{ox}e^{-\lambda_x D}$ $(m^{-1}\ m^{-3})$. Due to the moment characteristics of the inverse exponential distribution, many quantities are directly related to the intercept and slope. For example, the total number concentration may be obtained as $N_x = n_{ox}/\lambda_x$, the arithmetic mean diameter as $\bar{D_x} = 1/\lambda_x$, and the median volume diameter is $D_{ox} = 3.67/\lambda_x$. Therefore, for a fixed slope value, increasing n_{ox} adds to the total number concentration of hydrometeors per volume. Decreasing (increasing) the slope parameter λ_x will increase (decrease) the distribution mean or median volume diameter. Cloud water and cloud ice are assumed to be of a single, uniform size.

Nearly all of the microphysical source and sink terms described by Lin et al. (1983) or Rutledge and Hobbs (1983) require distribution characteristics in order to parameterize the effects of aggregation, depositional growth, and other terms. The evolution of water mass among the simulated species is highly dependent upon the distribution characteristics prescribed within a particular model forecast and single-moment scheme. Within the GSFC formulation, fixed intercepts are used for all precipitating classes, while the

WSM6 scheme varies the snow intercept parameter as a function of temperature (Table 1), based on observations by Houze et al. (1979). Mass-weighted terminal velocities and the collection efficiencies for snow and cloud water or ice also vary among these schemes. In addition, the WSM6 auto-converts snow to graupel when the snow mixing ratio exceeds a threshold value of 0.6 $g\ kg^{-1}$. Cloud ice sedimentation is not present within GSFC but is carried out within the WSM based upon mass and fall speed characteristics for bullet-type crystals. These differences accumulate with each model time step and contribute to some significant differences in profiles of mean hydrometeor content and reflectivity characteristics addressed in future sections.

3. Overview of the Super Tuesday Outbreak

During the period of 5-6 February 2008, a deep and progressive mid-level trough (500 hPa) traversed the central United States, driving the northward advection of warm, moist air to establish significant instability, shear, and an elevated mixed layer across the southeastern United States (Crowe and Mecikalski 2008). Specifically, observations on 1200 UTC 5 February 2008 depicted a surface low in central Oklahoma with a nearly stationary boundary stretching northeast toward the Midwest and Great Lakes (Fig. 1). This slow moving cold front provided a forcing mechanism for persistent convection extending from Illinois through Pennsylvania. As the upper-level trough entered the Great Plains (not shown), the Oklahoma surface low trended northeastward, and the attendant cold front focused a narrow, intense squall line and numerous long-lived, cyclic supercells responsible for significant damage deeper into the southeastern United States, spawning the majority of the 87 tornadoes and damaging wind or hail reports confirmed during the event.

The components of the Super Tuesday Outbreak of interest here are sensitivities in quantitative precipitation forecasts (QPF) and radar characteristics of cold frontal convection simulated during the outbreak. Based on Weather Surveillance Radar-1988 Doppler (WSR-88D) radar mosaic imagery, convection of varying strength and organizational mode was widespread during the 36 hour period, 0000 UTC 5 February to 1200 UTC 6 February 2008. This event provides an opportunity to examine the microphysical properties of simulated phenomena, resulting forecasts and sensitivities.

Table 1. Size Distribution Characteristics of the GSFC and WSM6 Schemes Utilized in WRF Model Forecasts

Scheme	Category	n_{ox} (m^{-4})	ρ_x (kg m^{-3})
GSFC	Rain	$8.0x10^6$	1000
	Snow	$1.6x10^7$	100
	Graupel	$4.0x10^6$	400
	Hail	$2.0x10^5$	917
WSM	Rain	$8.0x10^6$	1000
	Snow	$2.0x10^6 e^{0.12(T_o - T)}$	100
	Graupel	$4.0x10^6$	500

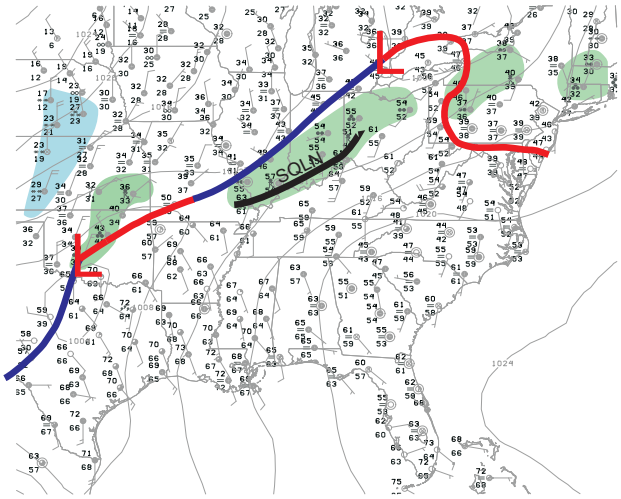

Fig. 1. Depiction of surface conditions at 1200 UTC 5 February 2008 with 1200 UTC NAM initialization isobars at 4 hPa interval. Green (blue) shading represents areas of rainfall or thunderstorms (snow). The position of an active squall line is marked 'SQLN' and maintained intensity through 1400 UTC and beyond, as referenced in the text.

4. Data and Methodology

a. *Weather Research and Forecasting (WRF) Model*

The WRF model is used extensively to investigate meteorological phenomena and perform real-time simulations within operational centers. Here, the WRF model is used to determine the sensitivities in QPF and radar characteristics of organized convection attributed to the assumptions made within single-moment, bulk water cloud microphysics schemes. Three formulations are applied to forecasts of the Super Tuesday Outbreak: the WSM6 (WSM6, Hong et al. 2004), the NASA Goddard six-class scheme with graupel (GSFC6G, Tao et al. 2008), and the NASA Goddard six-class scheme with hail (GSFC6H, Tao et al. 2008). In order to evaluate model performance, the aforementioned simulations adopt the choices of additional parameterizations selected for use in experimental, real-time forecasts generated by the NSSL and utilized during the 2008 Spring Experiment (Table 2; National Severe Storms Laboratory 2008). Initial conditions provided by North American Mesoscale (NAM) model fields were a reasonable depiction of the synoptic scale environment, although a southward displacement of the Oklahoma surface low is apparent (Fig. 1).

b. *Precipitation Verification*

Comparisons between observed precipitation rates and modeled counterparts are made using the NCEP Stage-IV hourly precipitation analyses (Lin and Mitchell 2005). These analyses are mosaics of combined radar estimates, surface gauge corrections and quality control steps conducted by NOAA/NWS River Forecast Centers. The Stage-IV analyses are distributed on an approximate 4x4 km grid, and quantitative verification is made after interpolating WRF output to the common Stage-IV grid (Fig. 2). Hourly fields of accumulated precipitation were obtained from 0000 UTC February 5 to 1200 UTC February 6 and are assumed to be

representative when assessing the performance of individual WRF forecasts.

c. Calculation of WRF Model Radar Reflectivity

Radars are heavily utilized in the observation and assessment of convective storm structure and precipitation, and radar reflectivity is often evaluated in the model output (Kain et al. 2008). Simulated radar reflectivity is calculated here following the methodology of Stoelinga (2005), similar to analyses performed by Smedsmo et al. (2005), and described in the Appendix. Manual calculation of radar reflectivity ensures that all scheme outputs are processed with appropriate distribution assumptions.

d. Application of WSR-88D Observations

The operational network of WSR-88Ds remotely sense the bulk properties of hydrometeors distributed within individual volume scans. Although the volume scanning strategy of a single, stationary radar limits the observations of an extensive squall line, multiple radars can be combined over time to provide a greater number of samples. Level II reflectivity was obtained from the National Climatic Data Center archives for radars that observed cold frontal convection from 1330-1430 UTC on 5 February 2008 (Fig. 2). Individual volume scans were edited to remove returns extraneous to the squall line of interest, then interpolated to a Cartesian grid with horizontal and vertical resolutions of 4 km and 500 m, respectively. Radar returns beyond a range of 200 km were ignored. Reflectivity from all radars and sampling time periods were aggregated into contoured frequency with altitude diagrams (CFADs, Yuter and Houze 1995) using histogram binning intervals of 4 dBZ on each vertical level. The CFAD technique provides a normalized histogram at a fixed altitude, and may be thought of as being similar to a probability density function. These WSR-88D CFADs provide a quantitative and qualitative assessment of the vertical distribution of reflectivity within the observed squall line and a basis for comparisons to the WRF simulated counterpart.

Table 2. Parameterizations used in the NSSL 2008 Spring Experiment WRF Model Configuration.

Physical Process	Parameterization Scheme
Boundary Layer	Mellor-Yamada-Janjic Scheme
Longwave Radiation	Rapid Radiative Transfer
Shortwave Radiation	Dudhia Scheme
Land Surface Processes	NOAH Land Surface Model
Cloud Microphysics	WSM6/GSFC6G/GSFC6H
Model Grid Characteristics	
Horizontal Spacing	4 km CONUS (980x750)
Vertical Levels	35 with varied spacing
Model Time Step	24/24/20 sec.

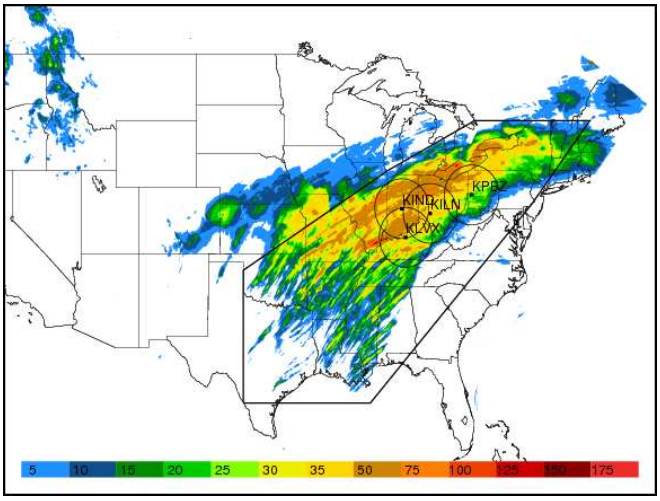

Fig. 2. Coverage area of the NSSL WRF model forecast domain and 36 hour accumulation of precipitation (mm) ending 1200 UTC February 6 2008, as estimated by NCEP Stage-IV analyses. Radars utilized in comparisons of observed and simulated cold frontal convection are noted by identifier and range ring containing utilized data. The inset polygon represents the portion of the WRF model and Stage-IV domains used in the processing of rain rate histograms.

5. RESULTS

a. Rain Rate Comparisons

Rain rate histograms of NCEP Stage-IV data depict two distinct time periods with higher precipitation rates, separated by a three hour minimum from 1500-1800 UTC on 5 February 2008 (Fig. 3). Precipitation rates in the first period were driven by the development and maintenance of cold frontal convection extending from Illinois to Pennsylvania. Around 1500 UTC, this convection temporarily weakened, while new development occured in the Central Plains. Beyond 1800 UTC, Central Plains convection continued to intensify and organize toward an intense squall line extending from Illinois to Texas. With all events combined, peak rain rates frequently exceeded 40 $mm\ h^{-1}$ during the 36 hour analysis period.

Among the graupel schemes (GSFC6G and WSM6), extremes in precipitation rate were generally underforecast. Peak hourly rain rates for cold frontal convection in the GSFC6G forecast were typically less than 24 $mm\ h^{-1}$, and although the WSM6 scheme produced higher intensity peak rates, they did not approach the extremes represented in Stage-IV analyses (Fig. 3). When hail distribution parameters are used instead of graupel (GSFC6H versus GSFC6G), precipitation rates are clearly enhanced, demonstrated by increases in maximum values and the frequency of rates above 40 $mm\ h^{-1}$. Although no severe hail was reported during this period, radar returns indicate that the convective line was vigorous and nearly steady state, likely producing large graupel and small hail. The GSFC6H configuration was likely more applicable within this portion of the domain, capable of distributing condensed water into the snow, cloud water and eventually hail categories. The conversion of water mass to the hail category would imply an increased terminal fall speed and translate to a greater rain rate, supporting the increased skill of the GSFC6H forecast as measured

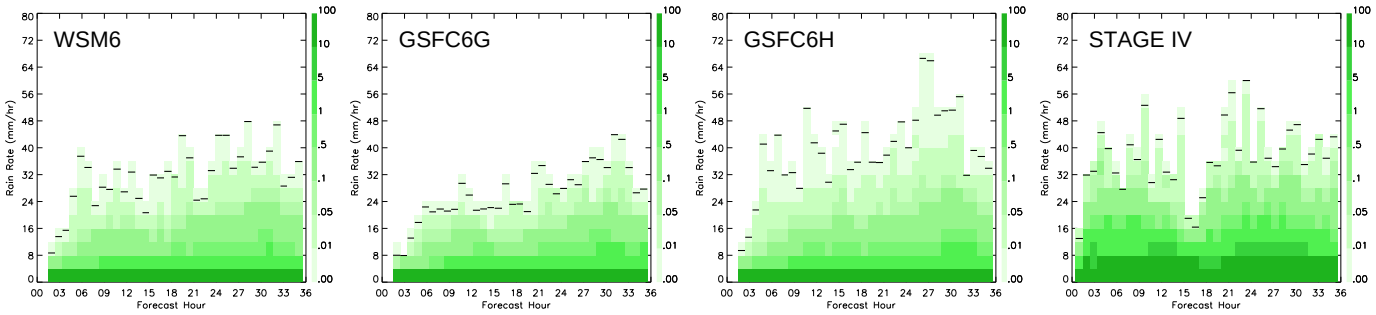

Fig. 3. Histograms of hourly rain rate (4 $mm\ h^{-1}$ interval) for WRF model and Stage-IV grid points contained within the polygon outlined in Fig. 2. Hourly maximum values are marked with a horizontal bar. Shading indicates percentage frequency with colors chosen to highlight the tails of extreme values within each probability density function.

by enhanced hourly rain rates that occur throughout the forecast cycle (Fig. 3). However, as a cold season case, hail distribution parameters and processes are likely to be inappropriate outside of the warm sector where stratiform rainfall and light to moderate snowfall were more frequent.

b. Object Based Verification Statistics

The WRF Verification Working Group has developed a package of statistical tools that incorporate object-based metrics, which accommodate a comparison of simulated phenomena despite errors in position or coverage area. Here, the Model Evaluation Tools (MET) package matches one hour accumulated precipitation to a comparable model forecast and identifies regions for appropriate comparison (Fig. 4). All WRF forecasts produce an appropriate coverage of precipitation throughout the Midwest, but with some excess in the Northeast. Cold frontal convection from Illinois to Pennsylvania is displaced approximately 50 km to the northwest in all forecasts, either a result of integrated errors in NAM boundary and initial conditions or model feedbacks between parameterized processes and the evolving mesoscale patterns. Convection in eastern Kansas, eastern Oklahoma and western Missouri is underforecast in coverage and intensity. The identification of "objects" may provide a situational awareness tool for model performance by highlighting similar deficiencies, especially for end users that are provided with a large number of model forecasts. In addition, the MET tool provides numerical guidance regarding forecast performance. A summary of selected forecast and observed parameters are provided in Table 3. Although the forecast coverage area of cold frontal precipitation is excessive, in this case much of it is driven by the erroneous inclusion of model activity in and north of Maine. Conversely, model forecasts of Central Plains convection produced roughly half as much coverage versus observations. Precipitation sensitivities to microphysics assumptions are still apparent, however, as the GSFC6H scheme provides a consistent increase in high intensity rain rates (90th percentile), although neither scheme is able to match the NCEP Stage IV intensities. Unfortunately, error uncertainty contributions from WSR-88D Z-R relations limit the viability of direct comparisons, but it is reasonable to assume that a hail scheme would improve the simulation

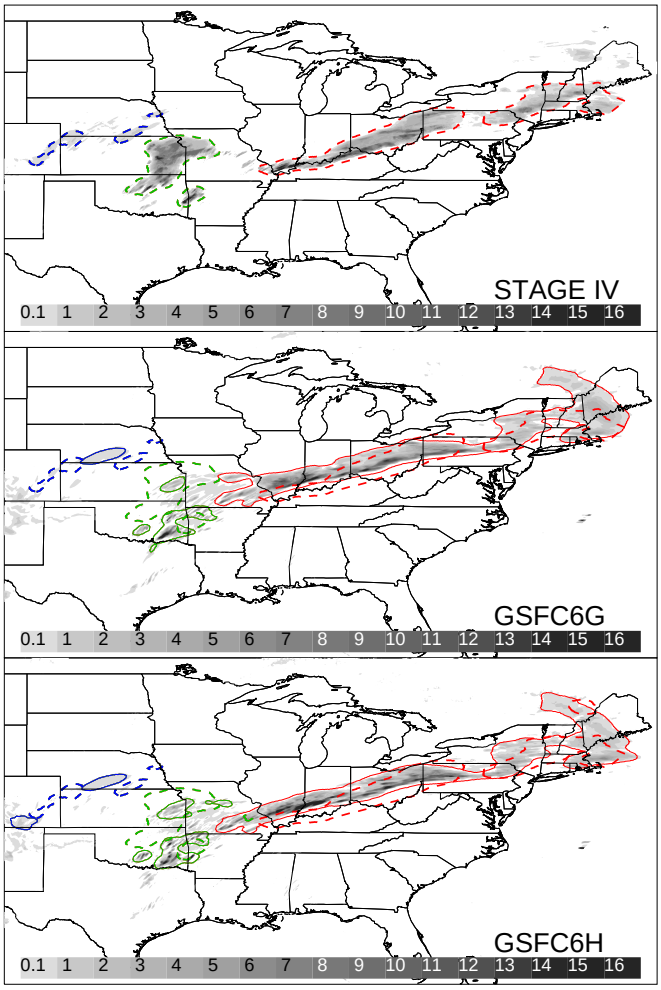

Fig. 4. Observed (dashed) and forecast (solid) precipitation objects derived from NCEP Stage IV and WRF model simulations using single-moment microphysics schemes. Precipitation accumulations are over a one hour period ending 1400 UTC February 5 2008, shaded in millimeters. Red (green) outlines refer to cold frontal (general) convection with statistics provided in Table 3. Blue outlines depict an object area of snow, not discussed in text.

Table 3. Selected Parameters for Cold Frontal (CF) and General Convection (GEN) from Object Based Verification Metrics

Source		Stage-IV	GSFC6G	GSFC6H
Area (points)	CF	18199	26642	25320
50^{th} Pct. (mm)		2.63	2.05	2.04
90^{th} Pct. (mm)		7.37	6.49	6.90
Area (points)	GEN	8774	4618	5720
50^{th} Pct. (mm)		3.74	1.21	1.17
90^{th} Pct. (mm)		9.50	5.09	5.43

of QPF from convective storms even if severe hail was not reported at the surface.

c. Mean Hydrometeor Profiles

The fundamental goal of a bulk water scheme is the distribution of water mass among its constituent hydrometeor classes. Differences in the vertical distribution of hydrometeors are examined, obtained from model profiles representing active cold frontal convection (Fig. 5) at 1400 UTC 5 February 2008 (forecast hour 14, Fig. 6). The greatest variation among the graupel schemes (GSFC6G and WSM6) is within the snow category, where peak snow values approach 0.6 $g\ m^{-3}$ around 5 km in the GSFC6G versus 0.1 $g\ m^{-3}$ at 7 km in the WSM6. Similarly, large differences in snow contents were obtained by Tao et al. (2008) in simulations of a mesoscale convective system observed during the International H_2O Project campaign. The GSFC6G formulation uses a fixed snow distribution intercept, in contrast to a temperature dependent form in WSM6 that includes an autoconversion threshold to graupel (Table 1). This contributes to significant differences in snow microphysical processes as the WSM6 has temperature-dependent variability in distribution parameters and a sink to graupel based on a tunable, critical value. The differences in snow and graupel characteristics influence the resulting precipitation totals. A transition of mass to the graupel category will increase the downward flux of ice, as graupel is prescribed a greater density and increased terminal velocity in either scheme. This may partially explain the presence of enhanced precipitation rates within WSM6 versus GSFC6G, and again in GSFC6H, where the size distribution and fall speed characteristics of the hail class produce greater numbers of larger, faster falling hydrometeors.

d. Radar Reflectivity Characteristics

Ideally, the radar characteristics of simulated convective storms should be comparable to their observed counterparts. Differences must be noted and leveraged to improve their respective microphysics schemes. Radar reflectivity profiles are obtained from WRF hydrometeor content and distribution characteristics (see Appendix) and are compared to an hour of combined, spatially overlapping WSR-88D observations through the use of CFADs (Fig. 7).

Qualitatively, the WSR-88D observations contain a low level reflectivity mode of 26-30 dBZ, extending to an altitude of 4 km, then followed by a steady decrease of approximately 3.33 $dBZ\ km^{-1}$. Regardless of the microphysics scheme, simulated WRF reflectivity CFADs show an excessive frequency of echoes greater than 30 dBZ for altitudes above 4 km (Fig. 7). Although these differences could be attributable to the sampling of the squall line by the WSR-88Ds, a significant fraction of WSR-88D observations is obtained from a range of 4-8 km. Excessively high reflectivity aloft was noted by Lang et al. (2007) for a tropical squall line and was attributed to the erroneous presence of high density ice (graupel) retained aloft where sink processes are limited. Within the GSFC schemes, calculations of the reflectivity contributions from snow and graupel (not shown) indicated that snow was the dominant contributor from 4 to 10 km. Small amounts of graupel dominated the simulated reflectivity above 10 km, comparable to the analysis of Lang et al. (2007). Unfortunately, the CFAD comparisons presented here do not allow for the determination of precise locations of reflectivity excess within the real or simulated, three dimensional squall line. However, despite the limited inferences available, the WSM6 scheme avoids a persistent reflectivity mode in the 3 to 6 km layer. This significant difference occurs above the freezing level (approximately 3 km), where snow distribution characteristics are allowed to vary as a function of temperature. The WSM6 snow distribution parameterization is based upon observations by Houze et al. (1979), which were limited to temperatures generally warmer than -30^oC, and therefore may not be applicable at colder temperatures. In addition, all of the single moment schemes utilized here are confined to a single snow crystal habit (spheres of fixed density), despite observed changes in density and shape characteristics as a function of ambient supersaturation and temperature. These assumptions and limitations likely combine within the WSM6 simulation and reflectivity profiles to mitigate the reflectivity mode within the 3 to 6 km layer, but underestimates the median reflectivity profile at higher altitude (colder temperature) where the assumptions are less valid.

e. Application of a Temperature Based Parameterization

Due to the dominance of snow in mid-level reflectivity profiles of the GSFC schemes, and the relative success of the WSM6 scheme in limiting excessive reflectivity aloft (Fig. 7), it seems worthwhile to consider a change in the handling of the GSFC fixed snow intercept. Although the WSM6 scheme chose to parameterize the snow intercept n_{os} by temperature based on observation of frontal clouds by Houze et al. (1979), another option is to allow for variations in the slope parameter λ_s, followed by a calculation of the intercept from the total available mass. Houze et al. (1979) provided a best fit line to parameterize λ_s as a function of temperature, and numerous field campaigns have provided similar equations (see Figure 2 of Ryan 2000). In addition, simulations of tropical convection using spectral bin schemes have suggested a temperature-based dependence for snow and graupel size distributions (T. Matsui, personal communication). Comparisons of CFADs are made between the default GSFC6G parameterization with fixed intercept, and

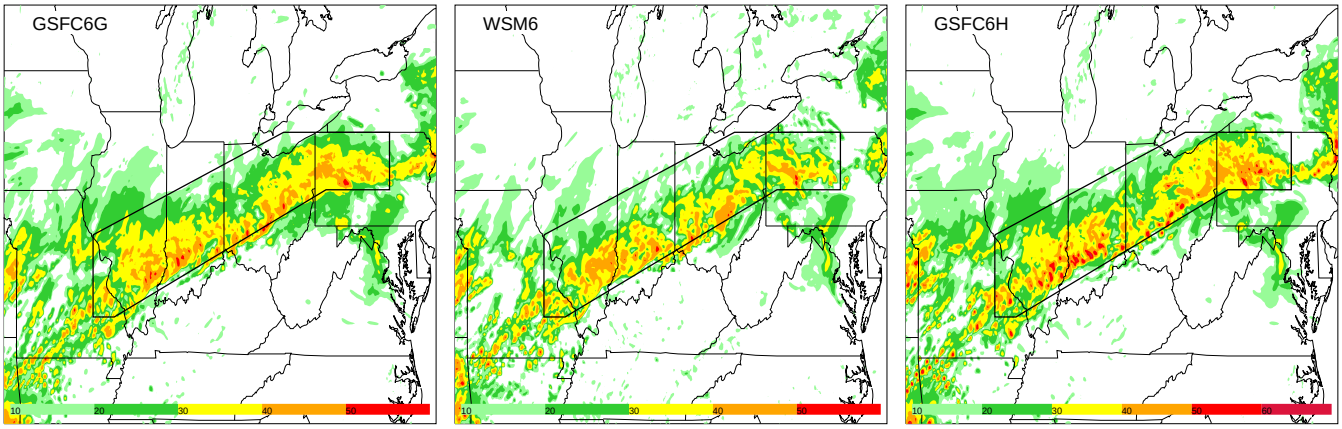

Fig. 5. Composite reflectivity (dBZ) based on WRF hydrometeor and temperature profiles for the forecast valid time of 1400 UTC February 5, 2008 (beginning of the 14^{th} simulation hour). The inset polygon outlines a subset of gridpoints used to calculate mean hydrometeor profiles and were also utilized to construct contoured frequency with altitude diagrams (CFAD, Yuter and Houze 1995) in subsequent figures.

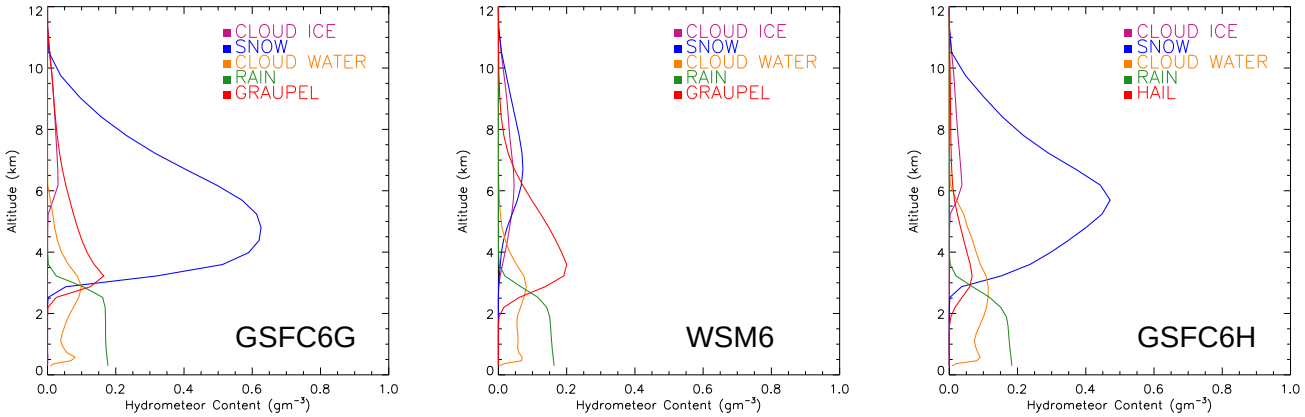

Fig. 6. Mean hydrometeor profiles obtained from WRF model forecasts of simulated cold frontal convection depicted in Fig. 5.

the parameterization $\lambda_s = 1220 \times 10^{0.0245(T_K - 273.16)} m^{-1}$ following Ryan (2000). This is equivalent to parameterizing the median volume diameter with altitude (recall $D_o = 3.67/\lambda$), given some lapse rate within the cloud profile. It is assumed that the profiles of simulated snow content are reasonable in magnitude, and therefore only changes in the size distribution are examined. In general, the inclusion of $\lambda_s(T)$ reduces the excessively high reflectivity above 4 km and adjusts toward the observed lapse rate in the median dBZ (see "RYAN" panel in Fig. 7). Above 3 km, errors in the median reflectivity profile are reduced, although modeled median reflectivity profiles significantly exceed WSR-88D observations above 8 km, regardless of any change. Graupel retains the fixed intercept method common to all schemes, and may remain a contributing factor to reflectivity excess as noted by Lang et al. (2007).

Although no conclusive judgment can be made based on a single case, it is apparent from the WSM6 simulation and application of $\lambda_s(T)$ to GSFC6G snow profiles that parameterizations of snow size distribution characteristics as functions of temperature (whether by intercept or slope) improve the match between observed and simulated reflectivity. Proper comparisons require the implementation of $\lambda_s(T)$ within the GSFC scheme and additional simulations for the Super Tuesday Outbreak. In addition, improvements to a single moment scheme require verification of hydrometeor content and size distribution parameters in terms of variables that are related to model output.

6. Summary and Conclusions

Three experimental forecasts of the Super Tuesday Outbreak were performed using the WRF model domain and configuration of the 2008 NSSL Spring Experiment. Varying microphysics schemes incorporated changes in hydrometeor class or the distribution characteristics of snow aggregates. Differences among the microphysics schemes contribute to variability in peak simulated rain rates and hydrometeor profiles, with the GSFC6H scheme providing the best representation of extreme rain rates within the warm sector. The WSM6 scheme generally produces greater rain rates than the GSFC6G scheme, attributable to an increase in graupel production (autoconversion from snow) which favors an increased, downward flux of ice mass owing to an increase in terminal velocity.

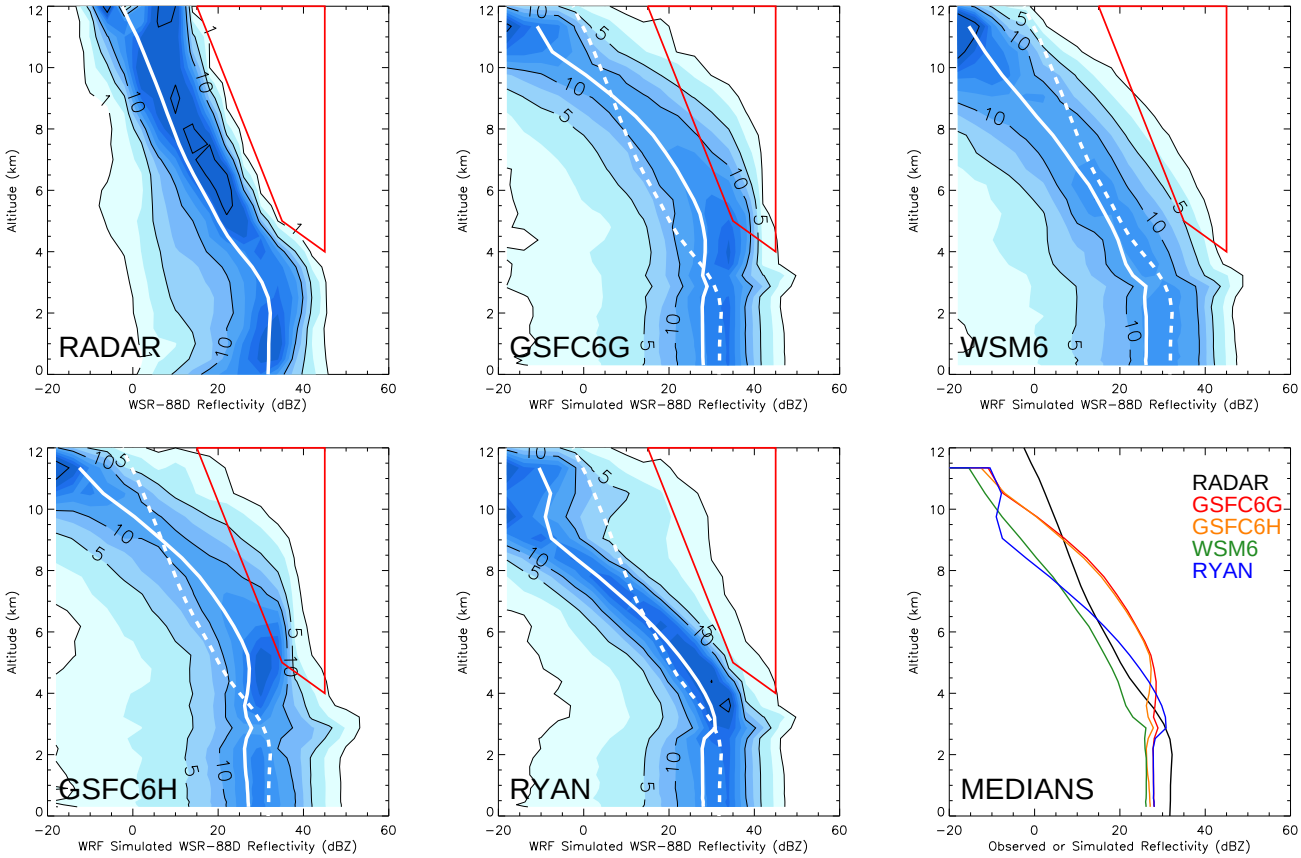

Fig. 7. Contoured frequency with altitude (CFAD, Yuter and Houze 1995) diagrams of observed and simulated radar reflectivity (dBZ) at WSR-88D frequency. The solid line in each panel is the respective median profile, while the RADAR median profile is replicated in model panels as a dashed reference line. Outlined areas represent a focal point for noted differences among radar observations and simulated reflectivity characteristics. The panel referenced RYAN incorporates hydrometeor profiles from the GSFC6G simulation with snow mass distributed by $\lambda_S(T)$ as described by Ryan (2000). Shading in CFADs is at 2.5% intervals with contours of 1%, 5%, 10% and 25% provided as a reference. The final panel, MEDIANS, provides a composite of all median reflectivity profiles among the CFADs presented here.

Simulated radar characteristics are often utilized to provide forecasters with a sense of storm intensity or mode, spurring comparisons against WSR-88D observations. While all schemes produced some occurrence of excessive reflectivity above 4 km, the WSM6 was best at mitigating this effect, likely a result of a snow size distribution that varies as a function of temperature. Other observational campaigns and spectral bin simulations support a temperature dependence, and a snow distribution slope parameterization (Ryan 2000) was explored based on an assumption that GSFC6G hydrometeor profiles are reasonable. Inclusion of this new parameterization mitigates excessive reflectivity aloft and is a step toward improving the match between simulated and observed radar characteristics. An ideal case for model verification would include estimates of hydrometeor size distribution characteristics and total available mass, in terms of spherical equivalent parameters applicable to the single-moment simulations. Future simulations will explore the use of $\lambda_S(T)$ parameterizations as integrated throughout the entire forecast cycle.

ACKNOWLEDGMENTS

Research described herein is accomplished using the resources and under the advisement of the Short-term Prediction Research and Transition (SPoRT) Center at NASA Marshall Space Flight Center (MSFC), Huntsville, Alabama. The authors would like to thank Dr. Wei-Kuo Tao of the Laboratory for Atmospheres at NASA Goddard Space Flight Center (GSFC), and Drs. Roger Shi and Toshi Matsui of the Goddard Earth Sciences and Technology Center at the University of Maryland Baltimore County for providing the current version of the Goddard microphysics scheme, guidance in installation, and discussion regarding the performance of the GSFC microphysics scheme.

Computational resources for this work were provided by the NASA Center for Computational Sciences at NASA GSFC. In addition, the lead author receives academic support and professional development opportunities through the Cooperative Education Program and Science and Mission Systems/Earth Science Office of NASA MSFC.

APPENDIX

CALCULATION OF RADAR REFLECTIVITY

1) Reflectivity Factor for Rain: Within the schemes utilized here, raindrops are assumed to fit the inverse-exponential size distribution $n(D) = n_{or}e^{-\lambda D}$. The equivalent radar reflectivity factor may be calculated as the sixth moment of the size distribution.

$$z_r = \int_0^\infty D^6 N(D) dD = \frac{720 n_{or}}{\lambda_r^7} \tag{1}$$

2) Equivalent Reflectivity Factor for Snow: As a frozen particle, two adjustments must be made for the calculation of an equivalent radar reflectivity factor: the particle size distribution must create solid ice targets of equivalent mass, and consideration made for the weaker dielectric constant associated with the ice crystal lattice. Given these modifications, the equivalent radar reflectivity factor for snow z_s can be calculated as

$$z_s = \left(\frac{\rho_s}{\rho_i}\right)^{\frac{1}{3}} \left(\frac{|K_{ice}|^2}{|K_{water}|^2}\right) \int_0^\infty D^6 N(D) dD \tag{2}$$

$$z_s = \left(\frac{\rho_s}{\rho_i}\right)^{\frac{1}{3}} \left(\frac{|K_{ice}|^2}{|K_{water}|^2}\right) \frac{720 n_{os}}{\lambda_s^7} \tag{3}$$

Stoelinga (2005) remarks that improvements could be made if the reflectivity calculation includes an effect for melting snowflakes and suggests using the dielectric constant for water in place of that for ice whenever snow crystals are present at temperatures above freezing. This will cause the reflectivity to increase by about 7 dBZ_e, and is implemented here as a separate reflectivity calculation for wet snow.

$$z_{sw} = \left(\frac{\rho_s}{\rho_i}\right)^{\frac{1}{3}} \frac{720 n_{os}}{\lambda_s^7} \tag{4}$$

3) Equivalent Reflectivity Factor for Graupel or Hail: The implementation of an equivalent reflectivity factor for graupel or hail is the same as the implementation for snow, except that distribution parameters vary based on the selection of graupel versus hail. The equivalent radar reflectivity factor for graupel (z_g) or hail (z_h) is calculated as:

$$z_g = \left(\frac{\rho_g}{\rho_i}\right)^{\frac{1}{3}} \left(\frac{|K_{ice}|^2}{|K_{water}|^2}\right) \frac{720 n_{og}}{\lambda_g^7} \tag{5}$$

$$z_h = \left(\frac{\rho_h}{\rho_i}\right)^{\frac{1}{3}} \left(\frac{|K_{ice}|^2}{|K_{water}|^2}\right) \frac{720 n_{oh}}{\lambda_h^7} \tag{6}$$

REFERENCES

Carbin, G. W. and J. T. Schaefer, 2008: The "Super Tuesday Tornado Outbreak" of February 5-6, 2008, SPC forecasts and historical perspective. *Preprints, 36th Conference on Broadcast Meteorology, Denver, CO, American Meteorological Society, P4.5.*

Crowe, C. and J. R. Mecikalski, 2008: Analysis of the elevated mixed layer during the Super Tuesday Outbreak. *Preprints, 24th Conference on Severe Local Storms, Savannah, GA, American Meteorological Society, 3A.4.*

Hong, S.-Y., J. Dudhia, and S.-H. Chen, 2004: A revised approach to ice microphysical processes for the bulk parameterization of clouds and precipitation. *Mon. Wea. Rev.*, **132**, 103–120.

Hong, S.-Y. and J.-O. J. Lim, 2006: The WRF single-moment 6-class microphysics scheme (WSM6). *Journal of the Korean Meteorological Society*, **42**, 129–151.

Houze, R. A., Jr., P. V. Hobbs, P. H. Herzegh, and D. B. Parsons, 1979: Size distributions of precipitation particles in frontal clouds. *J. Atmos. Sci.*, **36**, 156–162.

Kain, J. S., et al., 2008: Severe-weather forecast guidance from the first generation of large domain convection-allowing models: Challenges and opportunities. *Preprints, 24th Conference on Severe Local Storms, Savannah, GA, American Meteorological Society, 12.1.*

Lang, S., W.-K. Tao, R. Cifelli, W. Olson, J. Halverson, S. Rutledge, and J. Simpson, 2007: Improving simulations of convective systems from TRMM LBA: Easterly and westerly regimes. *J. Atmos. Sci.*, **64**, 1141–1164.

Lin, Y. and K. E. Mitchell, 2005: The NCEP Stage II/IV hourly precipitation analyses: Development and applications. *Preprints, 19th Conference on Hydrology, American Meteorological Society, San Diego, CA.*

Lin, Y.-L., R. D. Farley, and H. D. Orville, 1983: Bulk parameterization of the snow field in a cloud model. *J. Appl. Metr.*, **22**, 1065–1092.

National Severe Storms Laboratory, 2008: NSSL Real Time WRF Model Forecasts. URL `http://www.nssl.noaa.gov/wrf`, URL `http://www.nssl.noaa.gov/wrf`.

Rutledge, S. A. and P. V. Hobbs, 1983: The mesoscale and microscale structure and organization of clouds and precipitation in midlatitude cyclones. VII: A model for the "seeder-feeder" process in warm-frontal rainbands. *J. Atmos. Sci.*, **40**, 1185–1206.

Ryan, B. F., 2000: A bulk parameterization of the ice particle size distribution and the optical properties in ice clouds. *J. Atmos. Sci.*, **57**, 1436–1451.

Smedsmo, J. L., E. Foufoula-Georgiou, V. Vuruputur, F. Kong, and K. Droegemeier, 2005: On the vertical structure of modeled and observed deep convective storms: Insights for precipitation retrieval and microphysical parameterization. *J. Appl. Metr.*, **42**, 1866–1884.

Stoelinga, M. T., 2005: Simulated equivalent reflectivity factor as currently formulated in RIP: Description and possible improvements, Read/Interpolate/Plot Implementation Document.

Tao, W.-K., J. Shi, S. Chen, S. Lang, S.-Y. Hong, C. Peters-Lidard, S. Braun, and J. Simpson, 2008: Revised bulk-microphysical schemes for studying precipitation processes. Part I: Comparisons with other schemes. *Mon. Wea. Rev., submitted.*

Yuter, S. E. and R. A. Houze, Jr., 1995: Three-dimensional kinematic and microphysical evolution of Florida cumulonimbus. Part II: Frequency distributions of vertical velocity, reflectivity, and differential reflectivity. *Mon. Wea. Rev.*, **123**, 1921–1940.